

Revisiting the Impact of Stochastic Multicloud Model on the MJO Using Low-Resolution ECHAM6.3 Atmosphere Model

Libin MA

Key Laboratory of Meteorological Disaster of Ministry of Education, Joint International Research Laboratory of Climate and Environment Change, Collaborative Innovation Center on Forecast and Evaluation of Meteorological Disasters, Earth System Modeling Center, School of Atmospheric Science, Nanjing University of Information Science and Technology, China
State Key Laboratory of Severe Weather, Chinese Academy of Meteorological Sciences, China

Karsten PETERS

Max Planck Institut für Meteorologie, Deutsches Klimarechenzentrum GmbH, Germany

Bin WANG

Earth System Modeling Center, School of Atmospheric Science, Nanjing University of Information Science and Technology, China
Department of Atmospheric Sciences and International Pacific Research Center, School of Ocean and Earth Science and Technology, University of Hawaii at Manoa, Hawaii, USA

and

Juan LI

Key Laboratory of Meteorological Disaster of Ministry of Education, Joint International Research Laboratory of Climate and Environment Change, Collaborative Innovation Center on Forecast and Evaluation of Meteorological Disasters, Earth System Modeling Center, School of Atmospheric Science, Nanjing University of Information Science and Technology, China

(Manuscript received 12 October 2018, in final form 9 June 2019)

Abstract

Based on the preceding work, the influence of the stochastic multicloud model (SMCM) on the Madden–Julian oscillation (MJO) in the state-of-the-art ECHAM6.3 atmospheric general circulation model (AGCM) is further evaluated. The evaluation presented here is based on six recently proposed dynamics-oriented diagnostic metrics. Lag–longitude correlation maps of surface precipitation in the eastern Indian Ocean and West Pacific Ocean confirm the previously discovered improved representation of the MJO in the modified ECHAM6.3 model compared with the standard configuration. In fact, the modified ECHAM6.3 outperforms the default ECHAM6.3 in five of

Corresponding author: Bin Wang, Department of Atmospheric Sciences and International Pacific Research Center, School of Ocean and Earth Science and Technology, University of Hawaii at Manoa, 1860 East-West Road, POST Bldg. 401, Honolulu, Hawaii 96822, USA
E-mail: wangbin@hawaii.edu
J-stage Advance Published Date: 28 June 2019



the six MJO-related diagnostics evaluated here. In detail, the modified ECHAM6.3 (1) successfully models the eastward propagation of boundary layer moisture convergence (BLMC); (2) captures the rearward-tilted structure of equivalent potential temperature (EPT) in the lower troposphere and forward-tilted structure of EPT in the upper troposphere; (3) exhibits the rearward-tilted structure of equatorial diabatic heating in the lower troposphere; (4) adequately simulates the MJO-related horizontal circulation at 850 and 200 hPa and the 300 hPa diabatic heating structure. These evaluations confirm the crucial role of convective-parameterization formulation on GCM-simulated MJO dynamics and support the further application and exploration of the SMC concept in full-complexity GCMs.

Keywords Madden–Julian oscillation; ECHAM6.3 atmospheric model; stochastic multcloud model; eastward propagation of Madden–Julian oscillation; dynamics-oriented diagnosis

Citation Ma, L., K. Peters, B. Wang, and J. Li, 2019: Revisiting the impact of stochastic multcloud model on the MJO using low-resolution ECHAM6.3 atmosphere model. *J. Meteor. Soc. Japan*, **97**, 977–993, doi:10.2151/jmsj.2019-053.

1. Introduction

The Madden–Julian oscillation (MJO) is the most pronounced tropical intraseasonal mode of variability (Madden and Julian 1971, 1972; Zhang 2005; Waliser et al. 2012). It is characterized by a convective anomaly envelope propagating eastward for 30–80 days and mostly originates in the Indian Ocean, propagates eastward, and transverses the Maritime Continent and equatorial Pacific Ocean in about 5 m s^{-1} (Zhang 2013; Yoneyama et al. 2013; DeMott et al. 2015).

Over the past four decades, the dynamical and thermodynamical structures of the MJO have been well documented by observations and theoretical models (e.g., Madden and Julian 1971, 1972; Rui and Wang 1990; Weickmann et al. 1985; Wheeler and Kiladis 1999; Zhang and Dong 2004; Kiladis et al. 2005; Majda et al. 2007; Thual et al. 2014). Observation results have shown that the moist boundary layer gradually deepens at the east of the MJO convection center (Johnson et al. 1999; Tian et al. 2006), which is thought to be critical for the MJO's typical eastward propagation speed (Wang et al. 2018). Using the re-analysis data, Hsu and Li (2012) argued that the zonal asymmetry of low-level moisture relative to the MJO convection center favors the eastward propagation of MJO by potentially causing a more unstable stratification on the east of the MJO convection center. Using a theoretical model, Wang, B. et al. (2016) pointed out that the MJO structure is regulated by the trio-interaction among moisture, diabatic heating, and large-scale dynamics. Wang and Chen (2017) suggested that the asymmetries of the MJO, such as the relative intensity of low-level equatorial easterly winds associated with Kelvin wave and westerly wind associated

with Rossby wave, strongly relate to the convective schemes. Their result shows that stronger easterly winds associated with Kelvin wave induce faster eastward propagation of the MJO, which is consistent with other numerical results (Kang et al. 2013; Adames and Kim 2016).

How about the MJO simulation in the community of general circulation models (GCMs)? Previous studies pointed out that, although notable progresses have been made, realistic simulation of the MJO is still a big challenge for many current GCMs (e.g., Slingo et al. 1996; Sperber 2004; Hung et al. 2013; Jiang et al. 2015; Ahn et al. 2017). The failures related to the simulation of the MJO manifest themselves in misrepresentations of the slow eastward-propagating signals, seasonal cycle, spatial distribution, and convection–wind coupling (Slingo et al. 1996; Sperber et al. 1997; Sperber 2004). These shortcomings are affected by cumulus parameterization (Maloney and Hartmann 2001; Peters et al. 2017), resolution (Inness et al. 2001; Liess and Bengtsson 2004; Crueger et al. 2013), mean state (Slingo et al. 1996; Inness and Slingo 2003), and air–sea interaction (Wang and Xie 1997; Liu and Wang 2013; Tseng et al. 2015; Fu et al. 2016, 2017). The errors introduced by conventional cumulus parameterization into GCM simulations can, to some extent, be overcome by coupling a cloud-resolving model (CRM) with GCMs at the scale of the GCM grid to replace traditional cumulus parameterization. In this methodology, referred to as “super-parameterization”, the embedded two-dimensional CRM-based convection parameterization interacts with the GCM's large-scale dynamics and has the ability to enable the simulation of MJO-like signals in idealized models (Grabowski 2001, 2003), GCMs

(Randall et al. 2003; Arnold et al. 2015; Wang, S. et al. 2016), and numerical weather prediction models (Subramanian and Palmer 2017). Instead, of having to rely on a cumulus convection parameterization, Miura et al. (2007) used the global CRM NICAM (Nonhydrostatic Icosahedral Atmosphere Model; Satoh et al. 2008) and successfully simulated the slow eastward propagation of the MJO. Moreover, NICAM has the ability to predict MJO events with lead times of up to 1 month with realistic initial conditions (Miura et al. 2007; Miyakawa et al. 2014). The history and recent developments of CRM are reviewed by Guichard and Couvreux (2017). However, running a global CRM or superparameterized model is a computationally demanding approach, possibly limiting its applicability in global earth system models (ESMs) used for very long integrations.

Another approach to resolve the abovementioned issues of operational convection parameterization schemes is the stochastic multicloud model (SMCM) (Khouider et al. 2010), which is derived from the multicloud model of Khouider and Majda (2006a, b), and its coupling with the existing convection parameterizations in GCMs. The SMCM evolved out of the multicloud models introduced by Majda et al. (2007) and Khouider and Majda (2008a, b) and predicts, constrained by the background atmospheric state, the evolution of a cloud population (congestus, deep convection and stratiform) by means of a coarse-grained birth–death process developed in time using a Markov chain Monte Carlo method. Specifically, the SMCM predicts the area fraction of each cloud type per GCM grid box. Since its advent, the SMCM has successfully been applied to investigate the tropical convectively coupled equatorial waves (Frenkel et al. 2012, 2013), MJO in an aquaplanet GCM (Deng et al. 2015), and tropical intraseasonal variability in the NCEP Climate Forecast System, which is a state-of-the-art coupled ocean–atmosphere model (Goswami et al. 2017a, b, c). The SMCM has also been shown to adequately reproduce observed tropical convection (Peters et al. 2013). Based on the latter study, Peters et al. (2017) incorporated a modified version of the SMCM, i.e., tuned to observations and including an altered internal response function, into ECHAM6.3 (Stevens et al. 2013), a state-of-the-art atmospheric general circulation model (AGCM) used by many research groups (e.g., Cao et al. 2018). Their results had shown that coupling the SMCM with ECHAM6.3 produces a better MJO performance by analyzing and comparing the Hovmöller diagram of daily mean total surface rainfall, wavenumber–frequency–spectra of outgo-

ing longwave radiation, multivariate EOF analysis (Waliser et al. 2009), and MJO life cycle. However, these analyses do not cover all aspects related to MJO evaluation in GCMs. In order to completely evaluate the influence of the SMCM on the simulation of MJO in ECHAM6.3, a set of dynamics-oriented metrics proposed by Wang et al. (2018), which complement the standardized set of diagnostics of the US CLIVAR MJO Working Group, are applied in this study. These dynamics-oriented metrics are designed to judge whether a GCM captures the eastward propagation of MJO in accordance with reasonable physical processes.

2. Model description, experiment designs, and data

The subversion of ECHAM6.3 used in this study is ECHAM6.3.02 versus ECHAM6.3.01p3 used in the study by Peters et al. (2017). ECHAM6.3.02 is the atmospheric component of the third generation of the Nanjing University of Information Science and Technology Earth System Model (NESM3.0; Cao et al. 2018) and is the basis for the atmospheric component of MPI-ESM1.2 of the Max Planck Institute for Meteorology (Mauritsen et al. 2019). A mass-flux scheme (Tiedtke 1989) with the modification of penetrative convection (Nordeng 1994) is used for the cumulus parameterization in ECHAM6.3 (see Möbis and Stevens (2012) and Stevens et al. (2013) for an overview and Peters et al. (2017) for a detailed analysis of simulated convection). Coupling the SMCM with ECHAM6.3's convection scheme modifies the schemes' deep-shallow trigger and closure formulation according to the area fraction of deep convective clouds predicted by the SMCM while retaining the full interactivity of the convection with the remaining model dynamics and physics. Following Peters et al. (2017), in this study, the modification of deep convection is only invoked if the SMCM predicts that the area fraction of deep cloud is greater than zero; otherwise, the shallow convection is enforced in the default convection parameterization (see Appendix for a brief review). We have confirmed that salient features of the SMCM implementation shown in the study by Peters et al. (2017), e.g., the improved spatiotemporal coherence of tropical surface precipitation, are also present in this slightly different model version (not shown).

We chose not to use the SMCM-predicted congestus and stratiform cloud fractions in our implementation as this would require a major reformulation of ECHAM's mass-flux convection and large-scale cloud schemes. This is out of scope in the context of this work. A different implementation of the SMCM into a

Table 1. Pattern correlation coefficient (PCC) and normalized root-mean-square error (NRMSE) between observation and model results.

Diagnostic fields	T31L47		T63L47	
	ECHAM_CTRL	ECHAM_SMCM	ECHAM_CTRL	ECHAM_SMCM
	PCC (NRMSE)	PCC (NRMSE)	PCC (NRMSE)	PCC (NRMSE)
Propagation of precipitation (EIO)	0.14 (1.02)	0.76 (0.62)	0.15 (1.00)	0.70 (0.71)
Propagation of precipitation (WPO)	0.68 (0.67)	0.82 (0.54)	0.66 (0.69)	0.79 (0.58)
Propagation of BLMC (EIO)	0.11 (1.06)	0.73 (0.70)	0.15 (1.02)	0.78 (0.73)
Propagation of BLMC (WP)	0.62 (0.75)	0.80 (0.58)	0.73 (0.65)	0.82 (0.53)
Horizontal structure of U850	0.66 (1.01)	0.87 (0.76)	0.69 (0.88)	0.81 (0.66)
Vertical structure of EPT	0.66 (1.01)	0.87 (0.76)	0.70 (1.10)	0.75 (0.86)
Vertical structure of diabatic heating	0.61 (1.20)	0.82 (0.85)	0.67 (1.06)	0.71 (0.86)
Horizontal structure of 200 hPa divergence	0.68 (1.53)	0.78 (1.09)	0.75 (1.30)	0.80 (1.00)
Horizontal structure of 300 hPa diabatic heating	0.78 (0.98)	0.87 (0.80)	0.80 (0.90)	0.84 (0.75)
Vertical structure of eddy APE generation	0.40 (1.11)	0.55 (1.17)	0.59 (0.87)	0.68 (0.76)

comprehensive GCM (CFSv2, Goswami et al. (2017a, b, c)) took a more rigorous approach by removing the host model's mass-flux convection scheme and using prescribed heating and moistening profiles for all SMCM-simulated cloud types, thereby avoiding the need to account for adopting the mass-flux framework to accommodate multiple cloud types. The heating and moistening profiles are used in that implementation scale linearly with cloud area fractions.

We performed AMIP-type simulations at two different resolutions (T31L47 and T63L47) with the default ECHAM6.3 (named as ECHAM_CTRL) and the ECHAM6.3 coupled with SMCM (named as ECHAM_SMCM). The horizontal resolution of T63 (T31) is about $1.9^\circ \times 1.9^\circ$ ($3.875^\circ \times 3.875^\circ$), and the vertical resolution is 47 levels extending from the surface to 0.01 hPa. The AMIP-type experiment integrates from 1976 to 2014 with the forcing and boundary data from Coupled Model Intercomparison Project Phase 6 (CMIP6). The first three years are considered as spin-up phase. To keep the description and comparison concise, only the results of T31L47 are discussed in this study, to show that the SMCM also has a positive influence on even coarser resolution than T63L47 (as shown in the study by Peters et al. 2017). The results of SMCM at T63L47 resolution are summarized in Table 1 for completeness.

To evaluate the performance of the simulated MJO, the model results of CTRL and SMCM are separately compared with observations. We use daily precipitation data from the Global Precipitation Climatology

Project version 1.2 (GPCP; Huffman and Bolvin 2013) as reference, downloaded from <ftp://meso.gsfc.noaa.gov/pub/1dd-v1.2>. On the other hand, winds, air temperature, diabatic heating, and specific humidity data are obtained from ERA-Interim reanalysis (Dee et al. 2011). The reference datasets span from 1997 to 2013. To enable intrinsic representation of the MJO variability by the model and adequately explore the key processes relevant for the MJO simulation, the data of the model from 1979 to 2014 are used in this study. Moreover, all observations are interpolated to model grids to make a direct comparison between observations and model results. Prior to analysis, a band-pass (20–70 days) filter is applied to all variables. Then the resulting intraseasonal anomalies are analyzed for boreal winter only (November to April). Six dynamics-oriented diagnoses of Wang et al. (2018) are discussed:

- (1) lag–longitude regression of 925 hPa boundary layer moisture convergence (BLMC),
- (2) zonal asymmetry of 850 hPa wind fields,
- (3) zonal–vertical structure of equivalent potential temperature (EPT) and convective instability index,
- (4) vertical structure of diabatic heating along the equator,
- (5) horizontal structure of 200 hPa divergence and 300 hPa diabatic heating,
- (6) and vertical structure of available potential energy (APE) generation along the equator.

Two studying areas are chosen: one is in the eastern Indian Ocean (EIO) and the other in the western

Pacific Ocean (WPO). To demonstrate and emphasize the planetary scale of the MJO, we consider relatively large studying areas (EIO: 10°S–10°N; 80–100°E, WPO: 10°S–10°N; 130–160°E). Note that the results discussed in this study are relative to EIO unless stated otherwise.

3. Results

3.1 Annual mean precipitation

Implementation of the SMCM into ECHAM6.3 results in an imbalance in the top-of-atmosphere (TOA) energy budget. Peters et al. (2017) noted this but did not perform a retuning of the model. The model version used here was retuned in order to maintain TOA energy balance—mainly through parameters related to clouds (see Mauritsen et al. 2012 for details regarding the tuning of ECHAM6). The impacts of SMCM on global energy balance, global water balance, and tuning processes are summarized in another work (in preparation). The annual mean precipitation is briefly discussed here. Compared with the global annual mean of GPCP (2.68 mm day⁻¹), model results show larger global annual mean precipitation rate. They are 2.94 mm day⁻¹, 2.90 mm day⁻¹, and 2.86 mm day⁻¹ for ECHAM_CTRL, ECHAM_SMCM_ORI, and ECHAM_SMCM, respectively. Here ECHAM_SMCM_ORI represents the version ECHAM6.3 coupled with SMCM with default parameters as ECHAM_CTRL. ECHAM_SMCM represents the retuned version of ECHAM6.3, which includes the SMCM. The three model versions produce similar geographic distribution of the annual mean precipitation (pattern correlation coefficient (PCC), which is calculated between model simulation and observation, is 0.84 for the three model simulations). But ECHAM_SMCM_ORI and ECHAM_SMCM have larger root-mean-square error than ECHAM_CTRL, which is 1.15 mm day⁻¹ versus 1.07 mm day⁻¹.

Recalling the results shown by Peters et al. (2017), ECHAM_SMCM_ORI reduces the precipitation amount over land, especially over South America. Figure 1 depicts the difference among model results and observations. It shows that ECHAM_SMCM and ECHAM_SMCM_ORI have similar bias patterns (Figs. 1a, b). However, the retuning results in systematic increase of precipitation over land and the Maritime Continent, thereby reducing the dry biases compared with observations when using an untuned model version (Fig. 1a and Peters et al. 2017). At the same time, the precipitation distribution over the tropical Atlantic is improved by significantly reducing the overestimation of precipitation near the South Amer-

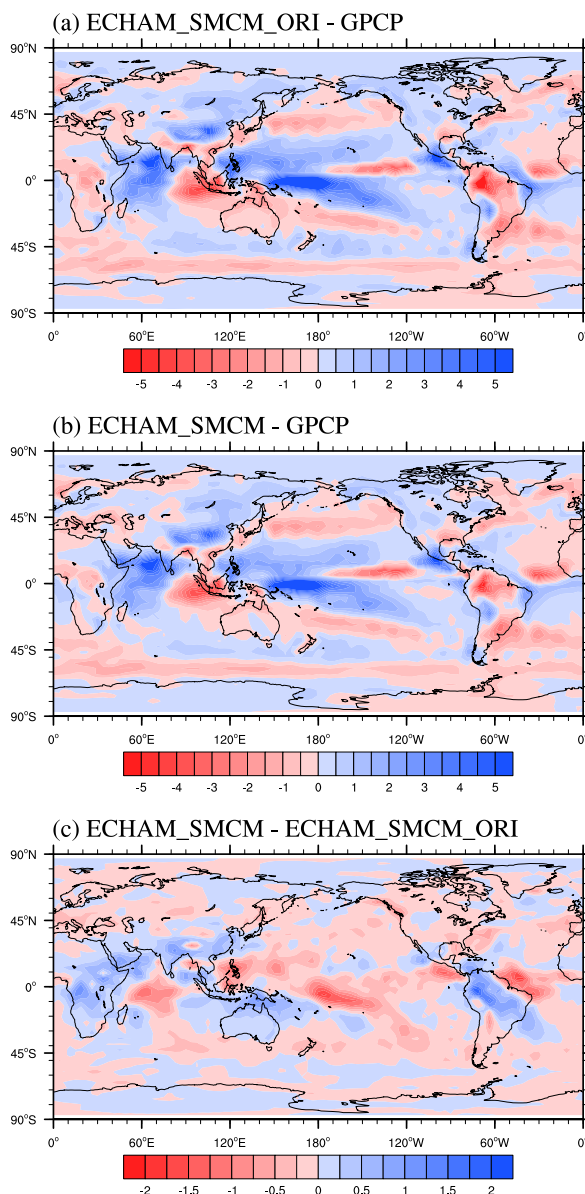


Fig. 1. Difference of annual precipitation (mm day⁻¹) of (a) ECHAM_SMCM_ORI and (b) ECHAM_SMCM T31L47 relative to GPCP. (c) Difference between ECHAM_SMCM and ECHAM_SMCM_ORI.

ican coast. The overestimation of precipitation in the South Pacific Convergence Zone seen in ECHAM_SMCM_ORI (Fig. 1a) is also reduced in ECHAM_SMCM (Figs. 1b, c). Thus, the following discussion focuses on the comparison between ECHAM_SMCM and ECHAM_CTRL.

3.2 Impact of SMCM on the eastward propagation of the MJO

The MJO most prominently manifests itself in a slow eastward-propagating envelope of organized deep convection, which is also key to its life cycle (Madden and Julian 1972). Thus, before exploring the influence of the SMCM on the MJO through the dynamics-oriented metrics, the impact of the SMCM on the eastward propagation of the MJO in ECHAM6.3 is firstly discussed here. Here, the eastward propagation of the MJO is straightforwardly depicted by the lag–longitude correlation of precipitation anomalies (Waliser et al. 2009). The averaged precipitation within the reference region (EIO or WPO) and 20–70-day filtered daily precipitation are used to conduct the lag–longitude correlation analysis.

Lag–longitude correlation maps of observed precipitation show that the MJO continuously propagates eastward from 50°E to 180°E referred to the precipitation in the EIO (Fig. 2a; e.g., Jiang et al. 2015; Wang et al. 2018). In ECHAM_CTRL, westward-propagating precipitation is simulated (Fig. 2b). ECHAM_SMCM shows eastward-propagating precipitation anomalies from 50°E to 140°E, indicating the presence of a simulated MJO-like disturbance. Although ECHAM_SMCM significantly improves the behavior of the eastward propagation of organized precipitation, i.e., the MJO, compared with ECHAM_CTRL (cf. Peters et al. 2017), it fails to capture the zonal extension of the propagation compared with observations (Fig. 2c). Using a different approach for the implementation of SMCM into a comprehensive GCM, Goswami et al. (2017c) found similar results (Fig. 4 in Goswami et al. (2017c)). Further, the reader is referred to the analysis of standard MJO diagnostics presented in the study by Peters et al. (2017), indicating that the performance of our implementation is comparable to other more direct implementations of the SMCM in comprehensive GCM frameworks (i.e., Goswami et al. 2017a, b, c).

To measure the performance of the simulated MJO in ECHAM_SMCM, the PCC and normalized root-mean-square error (NRMSE) between observations and model results are calculated. Here, the NRMSE is the RMSE between observations and model results normalized by the standard deviation of observations. As revealed by observation and model results, a local stationary oscillation of the MJO in the EIO mainly centers on the longitudinal range from 85°E to 95°E (e.g., Jiang et al. 2015; Wang and Lee 2017). Thus, to eliminate the stationary behavior of the MJO, the PCC and NRMSE are calculated within the time–longitude

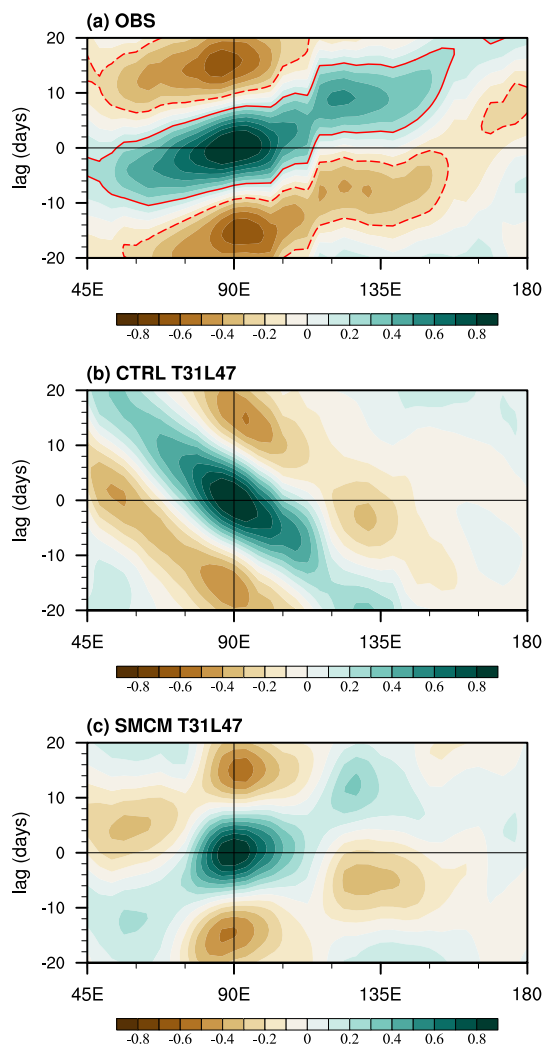


Fig. 2. Eastward propagation of MJO precipitation as indicated by the lead–lag correlation of 20–70-day filtered precipitation averaged over 10°S–10°N with reference to the precipitation at the equatorial eastern Indian Ocean (10°S–10°N, 80–100°E) during boreal winter (NDJFMA): (a) observation, (b) ECHAM_CTRL, and (c) ECHAM_SMCM. The red contour in (a) represents correlation coefficient (CC) of ± 0.2 .

domain (50–180°E, from day–20 to day 20), where the absolute correlation coefficient is greater than 0.2 within ± 20 days in the observation, excluding the longitude range from 85°E to 95°E (Wang et al. 2018). Due to the westward propagation of the MJO, ECHAM_CTRL has a very low PCC and large NRMSE, which are 0.14 and 1.02, respectively (Table 1). Consistent with the results shown by the lag–

longitude correlation map, ECHAM_SMCM has much better PCC (0.76) and NRMSE (0.62) scores (Table 1).

Besides comparing the eastward propagation of the MJO in the EIO, we also analyzed the propagation of the MJO in the WPO. Similar to the performance of the MJO in EIO, ECHAM_SMCM shows eastward propagation of the MJO in the WPO, whereas ECHAM_CTRL simulates westward-propagating precipitation anomalies (figures not shown here). The PCC and NRMSE scores confirm that ECHAM_SMCM has better performance than ECHAM_CTRL. As listed in Table 1, the PCC and NRMSE of ECHAM_SMCM (ECHAM_CTRL) are 0.82 (0.68) and 0.54 (0.67), respectively. The results are similar for T63L47 resolution (Table 1).

3.3 Dynamics-oriented diagnostic metrics

In this section, the impact of SMCM on the performance of simulated MJO is explored through the dynamics-oriented diagnostics proposed by Wang et al. (2018).

a. Boundary layer moisture convergence

Observational evidence and model results have shown that the boundary layer convergence may be a crucial factor determining the eastward propagation of the MJO (e.g., Maloney and Hartmann 1998; Wang, B. et al. 2016; Wang, S. et al. 2016; Wang and Lee 2017). Figure 3 depicts the propagation of BLMC at 925 hPa in the EIO. Similar to the propagation of precipitation, observations show that the BLMC signal systematically propagates eastward from 50°E to 180°E (Fig. 3a). BLMC, which compares well to the propagation of precipitation anomalies in the simulations (Figs. 2b, c), as simulated by ECHAM_CTRL and ECHAM_SMCM propagates westward and eastward, respectively (Figs. 3b, c). The PCC and NRMSE scores support the impression gained from Fig. 3 and confirm that SMCM T31L47 performs better than CTRL T31L47 in terms of the propagation of BLMC associated with the MJO. The results are similar when using the WPO as reference region. The comparison discussed here supports the view that better performance in simulating the propagation of BLMC reproduces realistic and better eastward propagation of the MJO in precipitation in the EIO and WPO (e.g., Wang et al. 2018). One would think that this should naturally be the case because organized precipitation in the tropics is associated with low-level convergence. So, nothing is really new here. However, that convection schemes often miss a link to large-scale dynamics and are closed on local thermodynamic quantities, e.g., con-

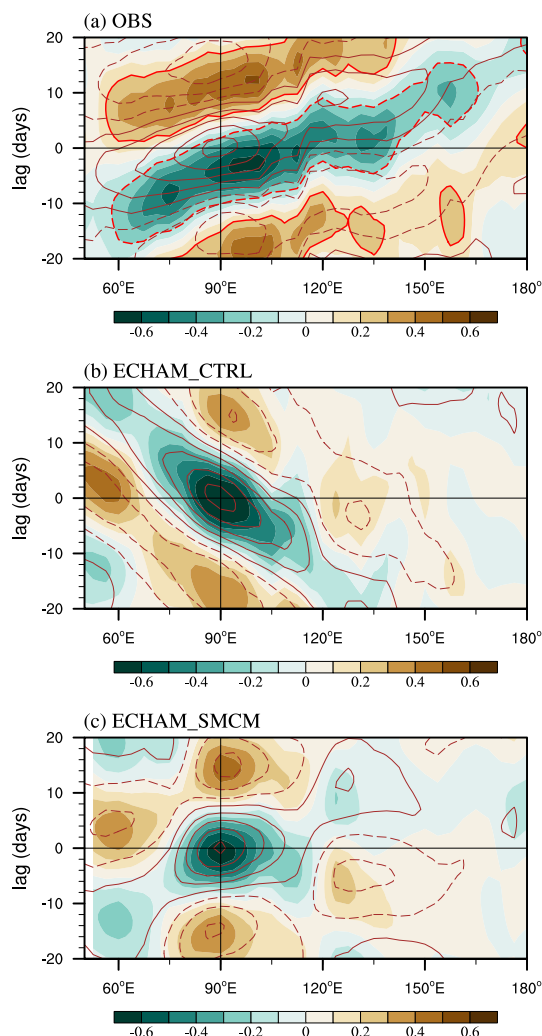


Fig. 3. Propagation of the boundary layer moisture convergence (BLMC) by the lead-lag correlation of 20–70-day filtered BLMC (day^{-1}) averaged over 10°S – 10°N with reference to the BLMC at the equatorial eastern Indian Ocean (10°S – 10°N , 80 – 100°E) of (a) observation, (b) ECHAM_CTRL, and (c) ECHAM_SMCM. The red contour in (a) represents correlation coefficient (CC) of ± 0.2 . The brown contours in (a), (b), and (c) represent the lag-longitude correlation map of precipitation.

vective available potential energy, has already been found in previous studies. This is not the case for the ECHAM_SMCM, which by implementation is coupled with large-scale dynamics at 500 hPa, showing its superior performance compared with ECHAM_CTRL.

b. 850 hPa horizontal circulation

The propagation of the MJO is closely related to the low-level wind circulation (Wang and Lee 2017) and intrinsically associated with the zonal extent and strength of Kelvin and Rossby waves (Gill 1980; Kang et al. 2013; Adames and Kim 2016; Wang, B. et al. 2016; Wang and Chen 2017). Figure 4a shows the horizontal circulation as obtained from the reanalyses at 850 hPa and the zonal asymmetry with westerlies and easterlies at the west and east of the major convection center, respectively. Both model results have similar features to those of the zonal asymmetry (Figs. 4b, c). However, there are some differences between the observation and model results. Compared with the observations, both model results have westward center of the Kelvin wave-induced easterly. The center of

the Kelvin wave-induced easterly of model results is located at the southern side of the equator, whereas the center of the Kelvin wave-induced easterly in observation appears at the north of the equator. Figure 4d shows the meridional average of the zonal wind in the latitudinal range from 5°S to 5°N. ECHAM_SMCM has the same zonal extent ratio between the Kelvin wave-induced easterly and Rossby wave-induced westerly (K-R), which is about 2.1, with that of observation. The zonal extent ratio of K-R of ECHAM_CTRL is only about 1.0. On the other hand, although ECHAM_SMCM has a comparable zonal extent ratio of K-R, it has a larger R-K intensity ratio, which is measured by the maximum speed of Rossby wave-induced westerly versus that of Kelvin wave-induced easterly. The R-K intensity ratios of observation

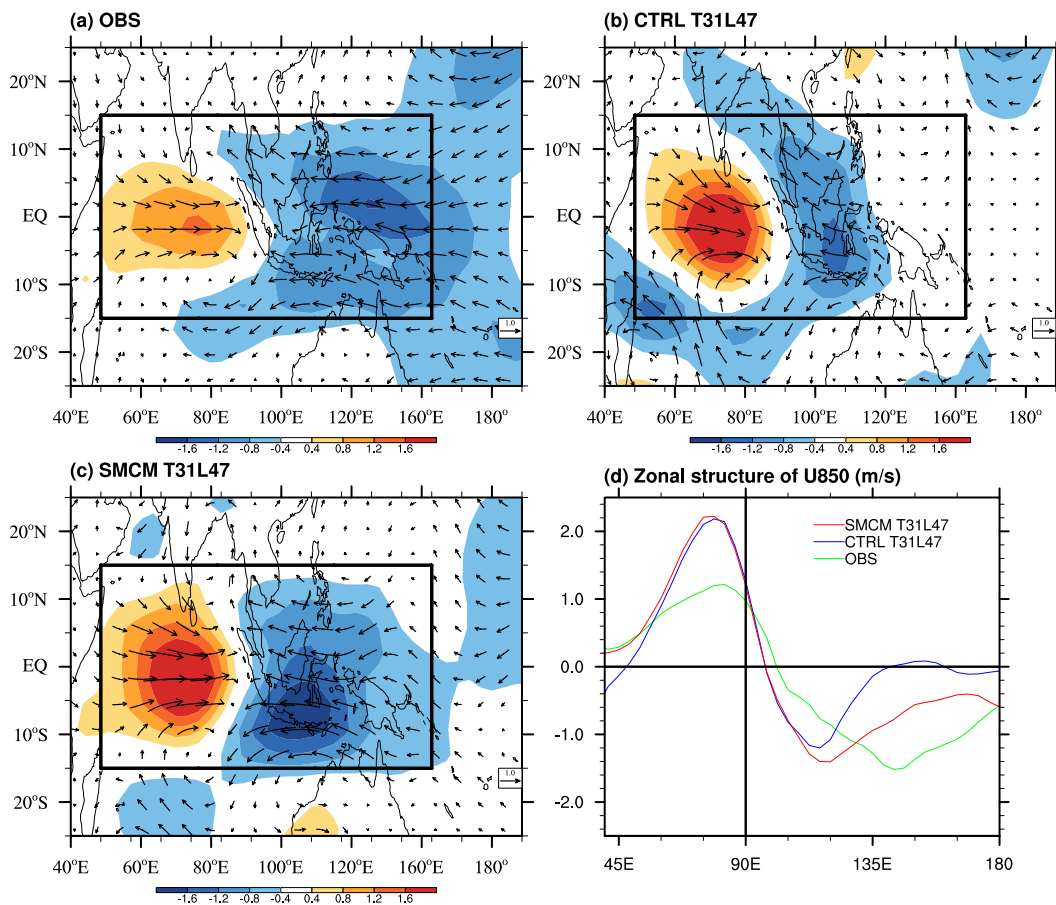


Fig. 4. Zonal asymmetry in the low-level circulation of 850 hPa winds (m s^{-1} ; vector) and zonal wind speed (m s^{-1} ; shading) of (a) observation, (b) ECHAM_CTRL, (c) and ECHAM_SMCM; (d) comparison of the longitudinal variations of the U850 in observation and model results. The structures are the 20–70-day filtered 850 hPa zonal winds and divergence regressed onto the 20–70-day filtered precipitation at the equatorial EIO (10°S–10°N and 80–100°E).

and ECHAM_SMCM are 0.8 and 1.4, respectively. Moreover, the R-K intensity ratio of ECHAM_CTRL is about 1.8. The superior performance of ECHAM_SMCM compared with ECHAM_CTRL in terms of capturing the MJO-associated low-level circulation is also confirmed by the PCC and NRMSE scores (Table 1).

c. Equivalent potential temperature structure

Figure 5 shows the structures of EPT anomalies, which are the meridional average between 5°S and 5°N. The maximum of EPT anomalies of observations and both model results is 500 hPa. Similar to the characteristics seen in observations, ECHAM_SMCM successfully models the tilted structure of EPT (Figs. 5a, c). From a low level to the height of 500 hPa, the EPT of ECHAM_SMCM illustrates a westward- and upward (rearward)-tilted structure. Then a reverse-tilted structure, which is eastward and upward, appears in the upper troposphere above 400 hPa. The low-

level rearward tilt favors a gradual deepening of the moist layer and moves westward relative to the major convection center and is thought to stimulate the eastward propagation of the MJO (e.g., Jiang et al. 2015). ECHAM_CTRL on the other hand does not indicate any tilted structure (Fig. 5b). As suggested in previous studies (e.g., Hsu and Li 2012; Wang and Lee 2017; Wang et al. 2018), we apply a convective instability index to measure the destabilization conditions of the atmospheric column with respect to deep convection to the east of the major convection center. To this end, the EPT difference between 850 and 400 hPa (850 hPa EPT minus 400 hPa EPT; Fig. 5d) is firstly calculated. Then, the convective instability index is calculated by averaging the previously computed difference in the longitudinal range from 120°E to 150°E. The convective instability indices of observation, ECHAM_CTRL, and ECHAM_SMCM are 0.39, 0.20, and 0.34, respectively, implying that ECHAM_SMCM captures the observed generation of high convective insta-

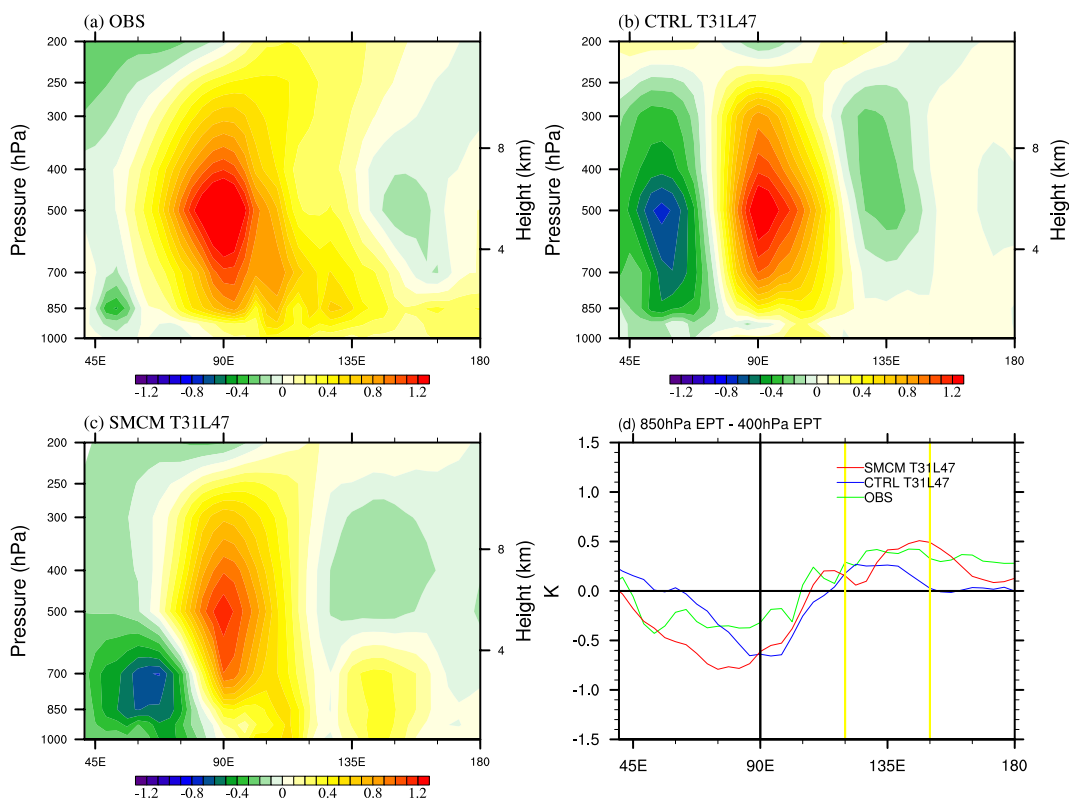


Fig. 5. Zonal asymmetry of the vertical structures of equivalent potential temperature anomalies (EPT; K) of (a) observation, (b) ECHAM_CTRL, (c) ECHAM_SMCM; (d) longitudinal variations of the difference of EPT between 850 and 400 hPa. The vertical structures are averaged between 5°S and 5°N, which are the 20–70-day filtered EPT fields regressed onto the 20–70-day filtered precipitation in the equatorial EIO (10°S–10°N, 80–100°E).

bility to the east of the MJO convection center, but ECHAM_CTRL fails to do so. Moreover, ECHAM_SMCM simulates the zonal asymmetry well (Fig. 5d). ECHAM_SMCM improvement is probably realized in terms of the modification of the deep convective trigger. Recall that Peters et al. (2017) showed that implementation of the SMCM into ECHAM6.3 leads to an increased number of shallow convective events, reaching deeper into the atmosphere—mimicking the effect of congestus cloud—potentially acting to precondition the atmosphere with regard to the occurrence of deep convection. ECHAM_SMCM improvement is also manifested by the PCC and NRMSE scores of EPT anomaly profiles, which are 0.87 and 0.76 versus 0.66 and 1.01 of ECHAM_CTRL, respectively (Table 1).

d. Vertical structure of diabatic heating

As shown in Fig. 6a, there is rearward (westward)-tilted structure in the lower troposphere of the diabatic heating as represented in the reanalysis, reminiscent of the deepening of convection as the MJO envelope propagates eastward. Note that vertical structures of diabatic heating of observation and model simulation shown in Fig. 6 are calculated by the meridional average between 5°S and 5°N . However, there is no such tilted structure simulated by ECHAM_CTRL (Fig. 6b), implying that ECHAM_CTRL probably fails to simulate the observed transition of cloud types, such as the transition from clear sky to congestus and shallow and congestus clouds to deep convective cloud. Although it is not as obvious as in the observations, ECHAM_SMCM successfully models the rearward-tilted structure in the lower troposphere (Fig. 6c). Both model results depict a narrowly trapped structure of diabatic heating compared with that of the reanalysis and demonstrate stronger diabatic heating. The ameliorated capacity of ECHAM_SMCM to simulate the zonal asymmetry of equatorial diabatic heating is confirmed by the PCC and NMRSE values (Table 1).

e. Upper-level divergence

Similar to the low-level horizontal divergence, the distribution of upper-level horizontal divergence can also be used to monitor the eastward propagation of the MJO (Adames and Wallace 2014). Figure 7 shows the horizontal distributions of winds and divergence at 200 hPa and the diabatic heating at 300 hPa. The observed upper-level circulation (vectors in Fig. 7a), which consists of the equatorial easterlies at the west of the convection center and the equatorial westerlies at the east of the convection center, shows the approximately out-of-phase relationship to that at

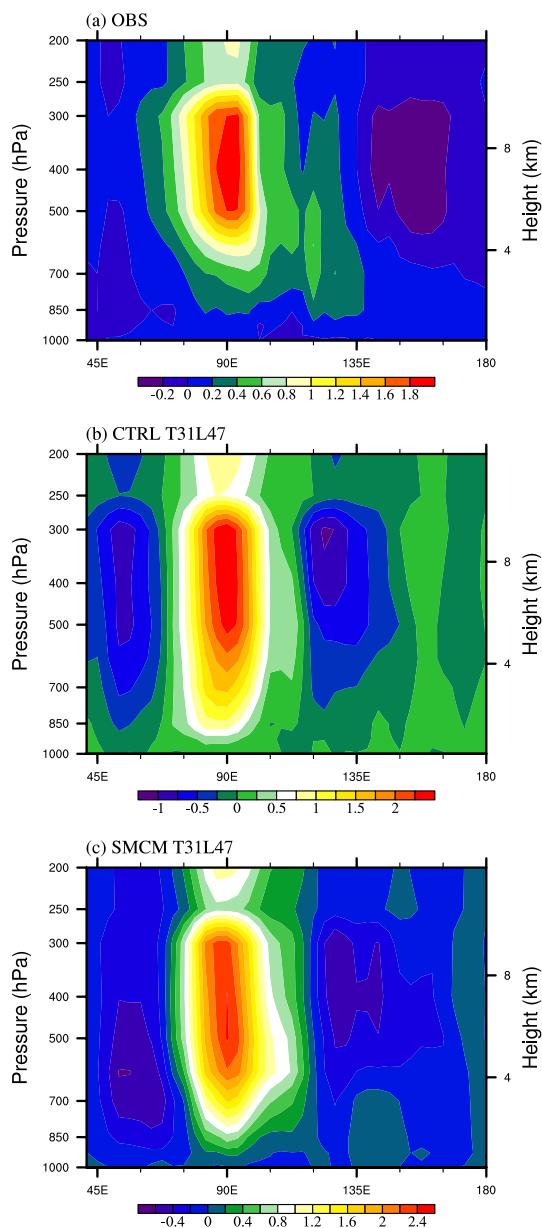


Fig. 6. Zonal asymmetry in diabatic heating (K day^{-1}) averaged between 5°S and 5°N in (a) observation, (b) ECHAM_CTRL, and (c) ECHAM_SMCM. The vertical structures are the 20–70-day filtered fields regressed onto 20–70-day filtered precipitation in the equatorial EIO (10°S – 10°N , 80 – 100°E).

850 hPa (vectors in Fig. 4a) (Wheeler and Hendon 2004; Waliser et al. 2009). The 200 hPa divergence is closely associated with the 300 hPa diabatic heating. Compared with the model result shown by ECHAM_

CTRL (Fig. 7b), ECHAM_SMCM largely simulates the observed 200 hPa wind pattern accompanying the westerlies at the east of the convection center and easterlies at the west of the convection center (Fig. 7c). However, there are some shortcomings. Like ECHAM_CTRL, there is no western extension of 200 hPa divergence and 300 hPa diabatic heating; instead, the 200 hPa divergence extends northeastward. Moreover, ECHAM_SMCM also shows stronger convergence at the east of the convection center than the reanalyses. The PCC and NRMSE of 200 hPa divergence and 300 hPa diabatic heating are calculated in the domain enclosed by black box (50–160°E and 15°S–15°N). As to 200 hPa divergence, the PCC and NRMSE of ECHAM_SMCM (EHCAM_CTRL) are 0.78 (0.68) and 1.09 (1.53), respectively. ECHAM_SMCM also outperforms ECHAM_CTRL with regard to 300 hPa diabatic heating (Table 1).

f. Vertical distribution of available potential energy

Figure 8 depicts the generation rate of vertical equatorial APE from 40°E to 180°E. As reported in other studies (e.g., Wang and Lee 2017; Wang et al. 2018), the observed APE generation rate exhibits significant zonal asymmetry relative to the MJO convection center in the lower troposphere (Fig. 8a). The generation rate of the MJO APE at the east of 90°E is greater than the one at the west of 90°E. As to the model results, both of them are capable of simulating the maximum center of APE generation rate at the upper troposphere as observation (Figs. 8b, c). However, both model results have poor simulation in the middle and lower troposphere (below 450 hPa) compared with observations. As shown in Fig. 8b, ECHAM_CTRL shows an interruption of the APE generation rate in the middle troposphere over the MJO convection center. After the modification of deep convection trigger through the SMCM implementation, ECHAM_SMCM is able to better represent the MJO APE generation rate at the east of the MJO convection center (Fig. 8c). But ECHAM_SMCM still fails to capture the observed vertical structure at the west of 90°E in the middle and lower troposphere. Furthermore, the PCC and NRMSE between simulated and observed APE generation rate calculated in the domain (40–180°E and 1000–200 hPa) are used to measure the simulation performance. The PCC and NRMSE of ECHAM_SMCM (ECHAM_CTRL) are 0.55 (0.40) and 1.17 (1.11), respectively.

4. Conclusions and discussion

As the follow-up work of Peters et al. (2017), the

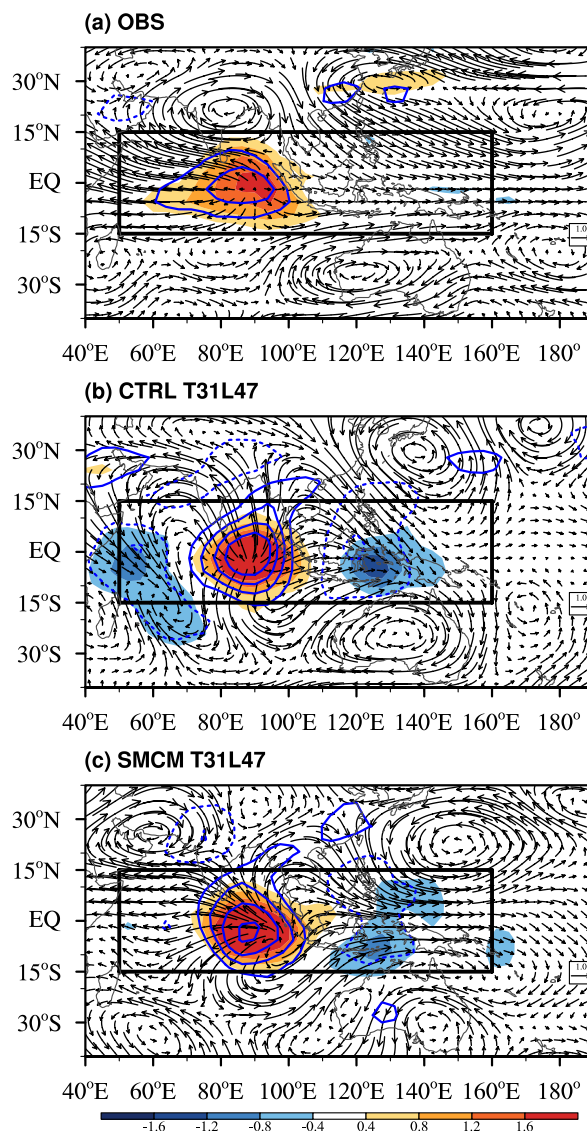


Fig. 7. The 200 hPa winds (m s^{-1} ; vector), divergence (day^{-1} ; contour), and 300 hPa diabatic heating (K day^{-1} ; shading) in (a) observation, (b) ECHAM_CTRL, and (c) ECHAM_SMCM. The structures are the 20–70-day filtered fields regressed onto the 20–70-day filtered precipitation at the equatorial EIO (10°S–10°N and 80–100°E).

influence of the SMCM on the capacity of the state-of-the-art GCM ECHAM6.3 to simulate the MJO is further evaluated in this study. Contrary to the model version discussed in the study by Peters et al. (2017), the model used here was retuned to maintain TOA radiation balance. This retuning significantly reduces

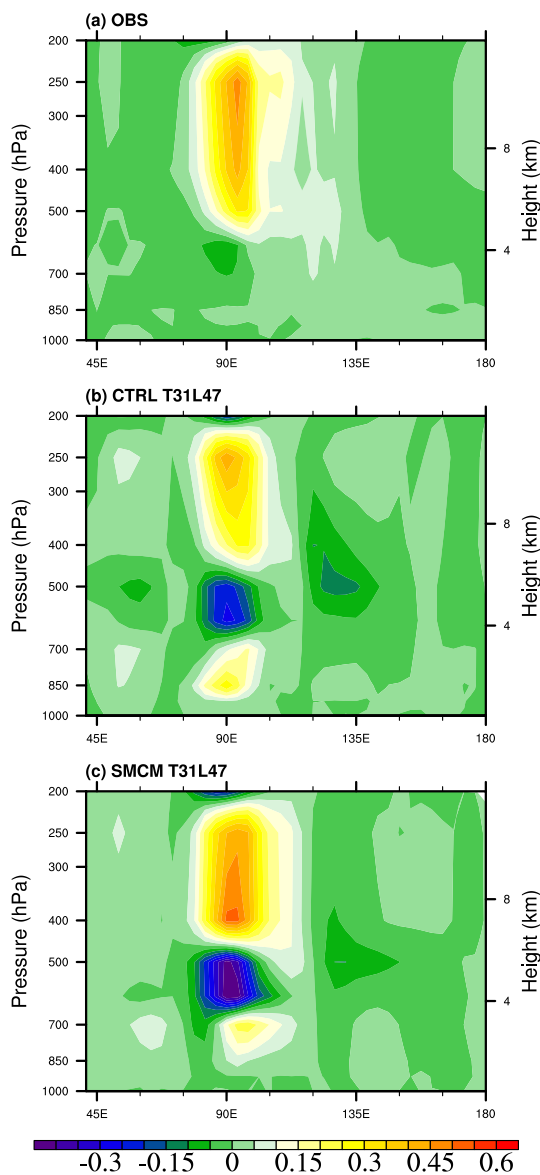


Fig. 8. Vertical structure of eddy available potential energy (APE) generation rate ($\text{K}^2 \text{day}^{-1}$) averaged between 5°S and 5°N in (a) observation, (b) ECHAM_CTRL, and (c) ECHAM_SMCM. The structures are the 20–70-day filtered APE fields regressed onto the 20–70-day filtered precipitation at the equatorial EIO (10°S – 10°N and 80 – 100°E).

the precipitation biases over tropical land masses reported in the study by Peters et al. (2017). Furthermore, model simulations at two different horizontal resolutions, T31 and T63, are analyzed here, with both setups having the same amount of vertical levels (47).

The analysis of lag–longitude correlation maps of precipitation in the EIO and the WPO clearly shows that the SMCM implementation results in the simulation of the MJO, whereas the standard model version cannot do so, thus confirming the results of Peters et al. (2017). Expanding on the analysis of Peters et al. (2017), the influence of the SMCM implementation on the MJO-dynamics is analyzed by applying six dynamics-oriented diagnostic metrics proposed by Wang et al. (2018).

The six dynamics-oriented metrics are (1) lag–longitude correlation of BLMC, (2) zonal asymmetry of low-level circulation (850 hPa), (3) vertical structure of the EPT and convective instability, (4) zonally asymmetric distribution of vertical diabatic heating, (5) zonal asymmetry of the upper-level divergence (200 hPa) and diabatic heating (300 hPa), and (6) generation of the MJO APE. Measured by PCCs and NRMSEs, it is obvious that ECHAM_SMCM outperforms the ECHAM_CTRL in terms of the first five dynamics-oriented metrics (Table 1). Notably, the benefits obtained by ECHAM_SMCM are clear by comparing the lag–longitude correlation of BLMC, zonal asymmetry of low- and upper-level circulation, vertical structure of the EPT and convective instability, and zonal asymmetry of vertical diabatic heating, whereas it is less clear in others. ECHAM_SMCM successfully simulates the observed eastward propagation of the BLMC, observed tilted structure of vertical EPT, and diabatic heating along the equator. In terms of the horizontal circulation at 850 hPa, compared with ECHAM_CTRL, ECHAM_SMCM has stronger Kelvin easterlies at the east of the MJO convection center and smaller R-K intensity ratio, which is thought to favor the eastward propagation of the MJO (e.g., Kang et al. 2013; Wang and Chen 2017). By comparing the 200 hPa winds, ECHAM_SMCM captures the observed features, depicting Rossby easterlies at the west and Kelvin westerlies at the east of the convection center.

By coupling the model SMCM with ECHAM6.3, only the trigger of deep convection and its closure, which is predicted by the model SMCM, is modified (Peters et al. 2017). This reformulation of the occurrence and strength of deep convection allows it to organize more realistically and, thus, couple more effectively with the large-scale dynamics, eventually resulting in the MJO simulation. Although coupling the SMCM with ECHAM6.3 improves the performance of simulated MJO in this study, there is still a long way to go to simulate it perfectly, such as the MJO's APE generation rate. Previous studies suggest-

ed that the shallow convection may exert significant influence on the simulation of the MJO (e.g., Thayer-Calder and Randall 2009; Tseng et al. 2015; Hirota et al. 2018). Additionally, congestus and stratiform cloud heating, which was first thoroughly studied in Majda and Shefter (2001) and took part in the conception of the multicloud model (Khouider and Majda 2006a), has been shown to play a vital role in the growth and propagation of the MJO (e.g., Mapes 2000; Kuang 2008a, b; Fu and Wang 2009). Both aspects are not covered by the SMCM implementation discussed here—there are noticeable impacts on the simulation of the shallow convection (Peters et al. 2017).

In fact, the SMCM predicts the temporal evolution of three cloud types: congestus, deep convective, and stratiform clouds (Khouider et al. 2010). Linearly scaled heating and moistening profiles of all three cloud types have been used for a more rigorous implementation of the SMCM into a comprehensive GCM (CFSv2, Goswami et al. (2017a, b, c)), which leads to ameliorated performance of that model in the simulation of synoptic and intraseasonal variability in the tropics. However, the analysis presented here, in support of Peters et al. (2017), shows that the SMCM also has the potential to provide the backbone of a new-generation mass-flux convection scheme calculating the occurrence of multiple convective clouds/updrafts alongside each other for use in GCMs—the benefit of which would be a complete integration into the host model’s dynamics and physics.

The following question then arises: Is it possible to further improve the performance of simulated MJO by fully coupling the SMCM with ECHAM6.3 or any other existing state-of-the-art GCM using the convective mass-flux approach? Given the results presented here and in previous studies, that question is worth investigating through investments in thorough model development in the future.

Acknowledgments

We thank Dr. Thorsten Mauritsen from Max Planck Institute for Meteorology on the suggestion of tuning the TOA imbalance. This work is supported by the National Key R&D Program of China (Grant No. 2018YFC1505803). This study is also sponsored by the Nanjing University of Information Science and Technology through funding the joint China-US Atmosphere-Ocean Research Center at the University of Hawaii at Manoa, and the Startup Foundation for Introducing Talent of NUIST (No. 2018r064). KP acknowledges funding by the Deutscher Wetterdienst

(DWD) within the Hans-Ertel-Zentrum for Weather Research (HERZ). This is IPRC publication number 1385 and the ESMC publication number 260.

Appendix

The incorporation of SMCM into ECHAM6.3 and the effects of SMCM on the convection are briefly described here. Readers can refer to Peters et al. (2017) for the details of the implementation of SMCM into ECHAM6.3.

To overcome the underestimation (overestimation) of convection for strong (weak) large-scale forcing, Peters et al. (2017) adopted a modified SMCM. In the modified SMCM, they replaced a function relating to the transition rate between different cloud types. The transition rate is exerted by the atmospheric large-scale state. The original function related to the transition rate (Khouider et al. 2010) has the following form:

$$\Gamma_1(x) = 1 - e^{-x}, \quad x \in [0, 2], \quad (\text{A1})$$

where x is C or D . C and D , which are the proxies for initiating and sustaining the deep convection and for midtropospheric dryness inhibiting the deep convection, respectively, are the two variables in the SMCM (Peters et al. 2013). Thus the transition rate can be formulated as $R_{ab} \propto \Gamma_1(C)\Gamma_1(D)$. Peters et al. (2013) pointed out the equation (A1) related to R_{ab} misrepresents the convective activity, which underestimates the convection for strong large-scale forcing and overestimates the convection for weak large-scale forcing. In the study by Peters et al. (2017), they adopted a tanh-related formulation:

$$\Gamma_2(x) = 0.52[0.964 + \tanh(2(x-1))], \quad x \in [0, 2]. \quad (\text{A2})$$

This modification enables the SMCM to simulate the observed behavior of convection (e.g., Peters et al. 2013).

The SMCM used in the study by Peters et al. (2017) and in this study aims to predict the base mass flux of the deep convective cloud. The base mass flux M_{cb} of deep convective cloud is formulated as as

$$M_{cb} = \sigma_d w_{cb} \rho_{cb}, \quad (\text{A3})$$

where σ_d is the area fraction of deep convection and w_{cb} and ρ_{cb} are the vertical upward velocity and the air density at cloud base, respectively. With the large-scale state variables relative humidity and vertical

pressure velocity at around 500 hPa, SMCM intends to predict σ_d . Combined with the default convective scheme used in ECHAM6.3, the SMCM modifies the deep, shallow convection trigger. If the convection is diagnosed and the predicted $\sigma_d > 0$, then deep convection is performed. If the convection scheme is invoked and $\sigma_d = 0$, then the shallow convection is performed.

How does the SMCM affect the convection? In-depth analysis by Peters et al. (2017) pointed out that the SMCM adopted in ECHAM6.3 improves (a) moisture–convection coupling, (b) spatiotemporal coherence of tropical daily rainfall, (c) representation of M_{cb} , (d) enhanced covariance of large-scale and convective precipitation, and (e) continuity of sub-daily deep convection. On the other hand, the SMCM suppresses the occurrence of deep convection at the places where it is not supported. This enables ECHAM6.3 coupled with SMCM to produce more realistic spatiotemporal coherence of daily rainfall at tropics. The improved spatiotemporal coherence of daily rainfall enhances the model capacity to simulate the MJO.

References

- Adames, A. F., and J. M. Wallace, 2014: Three-dimensional structure and evolution of the vertical velocity and divergence fields in the MJO. *J. Atmos. Sci.*, **71**, 4661–4681.
- Adames, A. F., and D. Kim, 2016: The MJO as a dispersive, convectively coupled moisture wave: Theory and observations. *J. Atmos. Sci.*, **73**, 913–941.
- Ahn, M.-S., D. Kim, K. R. Sperber, I.-S. Kang, E. Maloney, D. Waliser, H. Hendon, and WGNE MJO Task Force, 2017: MJO simulation in CMIP5 climate models: MJO skill metrics and process-oriented diagnosis. *Climate Dyn.*, **49**, 4023–4049.
- Arnold, N. P., M. Branson, Z. Kuang, D. A. Randall, and E. Tziperman, 2015: MJO intensification with warming in the superparameterized CESM. *J. Climate*, **28**, 2706–2724.
- Cao, J., B. Wang, Y.-M. Yang, L. Ma, J. Li, B. Sun, Y. Bao, J. He, X. Zhou, and L. Wu, 2018: The NUIST Earth System Model (NESM) version 3: Description and preliminary evaluation. *Geosci. Model Dev.*, **11**, 2975–2993.
- Crueger, T., B. Stevens, and R. Brokopf, 2013: The Madden–Julian oscillation in ECHAM6 and the introduction of an objective MJO metric. *J. Climate*, **26**, 3241–3257.
- Dee, D. P., S. M. Uppala, A. J. Simmons, P. Berrisford, P. Poli, S. Kobayashi, U. Andrae, M. A. Balmaseda, G. Balsamo, P. Bauer, P. Bechtold, A. C. M. Beljaars, L. van de Berg, J. Bidlot, N. Bormann, C. Delsol, R. Dragani, M. Fuentes, A. J. Geer, L. Haimberger, S. B. Healy, H. Hersbach, E. V. Hólm, L. Isaksen, P. Kållberg, M. Köhler, M. Matricardi, A. P. McNally, B. M. Monge-Sanz, J.-J. Morcrette, B.-K. Park, C. Peubey, P. de Rosnay, C. Tavalato, J.-N. Thépaut, and F. Vitart, 2011: The ERA-interim reanalysis: Configuration and performance of the data assimilation system. *Quart. J. Roy. Meteor. Soc.*, **137**, 553–597.
- DeMott, C. A., N. P. Klingaman, and S. J. Woolnough, 2015: Atmosphere–ocean coupled processes in the Madden–Julian oscillation. *Rev. Geophys.*, **53**, 1099–1154.
- Deng, Q., B. Khouider, and A. J. Majda, 2015: The MJO in a coarse-resolution GCM with a stochastic multcloud parameterization. *J. Atmos. Sci.*, **72**, 55–74.
- Frenkel, Y., A. J. Majda, and B. Khouider, 2012: Using the stochastic multcloud model to improve tropical convective parameterization: A paradigm example. *J. Atmos. Sci.*, **69**, 1080–1105.
- Frenkel, Y., A. J. Majda, and B. Khouider, 2013: Stochastic and deterministic multcloud parameterizations for tropical convection. *Climate Dyn.*, **41**, 1527–1551.
- Fu, J.-X., W. Q. Wang, T. Shinoda, H.-L. Ren, and X. Jia, 2017: Toward understanding the diverse impacts of air–sea interaction on MJO simulations. *J. Geophys. Res.*, **122**, 8855–8875.
- Fu, X., and B. Wang, 2009: Critical roles of the stratiform rainfall in sustaining the Madden–Julian oscillation: GCM experiments. *J. Climate*, **22**, 3939–3959.
- Fu, X., W. Wang, J.-Y. Lee, B. Wang, K. Kikuchi, J. Xu, J. Li, and S. Weaver, 2016: Distinctive roles of air–sea coupling on different MJO events: A new perspective revealed from the DYNAMO/CINDY field campaign. *Mon. Wea. Rev.*, **143**, 794–812.
- Gill, A. E., 1980: Some simple solutions for heat-induced tropical circulation. *Quart. J. Roy. Meteor. Soc.*, **106**, 447–462.
- Goswami, B. B., B. Khouider, R. Phani, P. Mukhopadhyay, and A. J. Majda, 2017a: Implementation and calibration of a stochastic multcloud convective parameterization in the NCEP climate forecast system (CFSv2). *J. Adv. Model. Earth Syst.*, **9**, 1721–1739.
- Goswami, B. B., B. Khouider, R. Phani, P. Mukhopadhyay, and A. J. Majda, 2017b: Improved tropical modes of variability in the NCEP climate forecast system (Version 2) via a stochastic multcloud model. *J. Atmos. Sci.*, **74**, 3339–3366.
- Goswami, B. B., B. Khouider, R. Phani, P. Mukhopadhyay, and A. J. Majda, 2017c: Improving synoptic and intraseasonal variability in CFSv2 via stochastic representation of organized convection. *Geophys. Res. Lett.*, **44**, 1104–1113.
- Grabowski, W. W., 2001: Coupling cloud processes with the large-scale dynamics using the cloud-resolving convection parameterization (CRCP). *J. Atmos. Sci.*, **58**, 978–997.
- Grabowski, W. W., 2003: MJO-like coherent structure: Sensitivity simulations using the cloud-resolving

- convection parameterization (CRCP). *J. Atmos. Sci.*, **60**, 847–864.
- Guichard, F. M., and F. Couvreux, 2017: A short review of numerical cloud-resolving models. *Tellus A*, **69**, 1, doi:10.1080/16000870.2017.1373578.
- Hirota, N., T. Ogura, H. Tatebe, H. Shiogama, M. Kimoto, and M. Watanabe, 2018: Roles of shallow convective moistening in the eastward propagation of the MJO in MIROC6. *J. Climate*, **31**, 3033–3047.
- Hsu, P.-C., and T. Li, 2012: Role of the boundary layer moisture asymmetry in causing the eastward propagation of the Madden–Julian oscillation. *J. Climate*, **25**, 4914–4931.
- Huffman, G. J., and D. T. Bolvin, 2013: *Version 1.2 GPCP One-Degree Daily precipitation data set documentation*. 27 pp. [Available at ftp://meso-a.gsfc.nasa.gov/pub/1dd-v1.2/1DD_v1.2_doc.pdf]
- Hung, M.-P., J.-L. Lin, W. Wang, D. Kim, T. Shinoda, and S. J. Weaver, 2013: MJO and convectively coupled equatorial waves simulated by CMIP5 climate models. *J. Climate*, **26**, 6185–6214.
- Inness, P. M., and J. M. Slingo, 2003: Simulation of the Madden–Julian oscillation in a coupled general circulation model. Part I: Comparisons with observations and an atmosphere-only GCM. *J. Climate*, **16**, 345–364.
- Inness, P. M., J. M. Slingo, S. J. Woolnough, R. B. Neale, and V. D. Pope, 2001: Organization of tropical convection in a GCM with varying vertical resolution: Implications for the simulation of the Madden–Julian Oscillation. *Climate Dyn.*, **17**, 777–793.
- Jiang, X., D. E. Waliser, P. K. Xavier, J. Petch, N. P. Klingaman, S. J. Woolnough, B. Guan, G. Bellon, T. Crueger, C. DeMott, C. Hannay, H. Lin, W. Hu, D. Kim, C.-L. Lappen, M.-M. Lu, H.-Y. Ma, T. Miyakawa, J. A. Ridout, S. D. Schubert, J. Scinocca, K.-H. Seo, E. Shindo, X. Song, C. Stan, W.-L. Tseng, W. Wang, T. Wu, X. Wu, K. Wyser, G. J. Zhang, and H. Zhu, 2015: Vertical structure and physical processes of the Madden–Julian oscillation: Exploring key model physics in climate simulations. *J. Geophys. Res.*, **120**, 4718–4748.
- Johnson, R. H., T. M. Rickenbach, S. A. Rutledge, P. E. Ciesielski, and W. H. Schubert, 1999: Trimodal characteristics of tropical convection. *J. Climate*, **12**, 2397–2418.
- Kang, I.-S., F. Liu, M.-S. Ahn, Y.-M. Yang, and B. Wang, 2013: Role of SST structure in convectively coupled Kelvin–Rossby waves and its implication for MJO formation. *J. Climate*, **26**, 5915–5930.
- Khouider, B., and A. J. Majda, 2006a: Model multi-cloud parameterizations for convectively coupled waves: Detailed nonlinear wave evolution. *Dyn. Atmos. Oceans*, **42**, 59–80.
- Khouider, B., and A. J. Majda, 2006b: A simple multcloud parameterization for convectively coupled tropical waves. Part I: Linear analysis. *J. Atmos. Sci.*, **63**, 1308–1323.
- Khouider, B., and A. J. Majda, 2008a: Multicloud models for organized tropical convection: Enhanced congestus heating. *J. Atmos. Sci.*, **65**, 895–914.
- Khouider, B., and A. J. Majda, 2008b: Equatorial convectively coupled waves in a simple multcloud model. *J. Atmos. Sci.*, **65**, 3376–3397.
- Khouider, B., J. Biello, and A. J. Majda, 2010: A stochastic multcloud models for tropical convection. *Commun. Math. Sci.*, **8**, 187–216.
- Kiladis, G. N., K. H. Straub, and P. T. Haertel, 2005: Zonal and vertical structure of the Madden–Julian oscillation. *J. Atmos. Sci.*, **62**, 2790–2809.
- Kuang, Z., 2008a: A moisture-stratiform instability for convectively coupled waves. *J. Atmos. Sci.*, **65**, 834–854.
- Kuang, Z., 2008b: Corrigendum. *J. Atmos. Sci.*, **65**, 3011–3011.
- Liess, S., and L. Bengtsson, 2004: The intraseasonal oscillation in ECHAM4. Part II: Sensitivity studies. *Climate Dyn.*, **22**, 671–688.
- Liu, F., and B. Wang, 2013: An air–sea coupled skeleton model for the Madden–Julian oscillation. *J. Atmos. Sci.*, **70**, 3147–3156.
- Madden, R. A., and P. R. Julian, 1971: Detection of a 40–50 day oscillation in the zonal wind in the tropical pacific. *J. Atmos. Sci.*, **28**, 702–708.
- Madden, R. A., and P. R. Julian, 1972: Description of global-scale circulation cells in the tropics with a 40–50 day period. *J. Atmos. Sci.*, **29**, 1109–1123.
- Majda, A. J., and M. G. Shefter, 2001: Models for stratiform instability and convectively coupled waves. *J. Atmos. Sci.*, **58**, 1567–1584.
- Majda, A. J., S. N. Stechmann, and B. Khouider, 2007: Madden–Julian Oscillation analog and intraseasonal variability in a multcloud model above the equator. *Proc. Nat. Acad. Sci. U. S. A.*, **104**, 9919–9924.
- Maloney, E. D., and D. L. Hartmann, 1998: Frictional moisture convergence in a composite life cycle of the Madden–Julian oscillation. *J. Climate*, **11**, 2387–2403.
- Maloney, E. D., and D. L. Hartmann, 2001: The sensitivity of intraseasonal variability in the NCAR CCM3 to changes in convective parameterization. *J. Climate*, **14**, 2015–2034.
- Mapes, B. E., 2000: Convective inhibition, subgrid-scale triggering energy, and stratiform instability in a toy tropical wave model. *J. Atmos. Sci.*, **57**, 1515–1535.
- Mauritsen, T., J. Bader, T. Becker, J. Behrens, M. Bittner, R. Brokopf, V. Brovkin, M. Claussen, T. Crueger, M. Esch, I. Fast, S. Fiedler, D. Fläschner, V. Gayler, M. Giorgetta, D. S. Goll, H. Haak, S. Hagemann, C. Hedemann, C. Hohenegger, T. Ilyina, T. Jahns, D. Jimenez-de-la-Cuesta, J. Jungclaus, T. Kleinen, S. Kloster, D. Kracher, S. Kinne, D. Kleberg, G. Lasslop, L. Kornbluh, J. Marotzke, D. Matei, K. Meraner, U. Mikolajewicz, K. Modali, B. Möbis, W. A. Müller, J.

- E. M. S. Nabel, C. C. W. Nam, D. Notz, S.-S. Nyawira, H. Paulsen, K. Peters, R. Pincus, H. Pohlmann, J. Pongratz, M. Popp, T. J. Raddatz, S. Rast, R. Redler, C. H. Reick, T. Rohrschneider, B. Stevens, J.-S. von Storch, F. Tian, A. Voigt, P. Vrese, K.-H. Wieners, S. Wilkenskjaeld, A. Winkler, and E. Roeckner, 2019: Developments in the MPI-M Earth System Model version 1.2 (MPI-ESM 1.2) and its response to increasing CO₂. *J. Adv. Model. Earth Syst.*, **11**, 998–1038.
- Mauritsen, T., B. Stevens, E. Roeckner, T. Crueger, M. Esch, M. Giorgetta, H. Haak, J. Jungclaus, D. Kloocke, D. Matei, U. Mikolajewicz, D. Notz, R. Pincus, H. Schmidt, and L. Tomassini, 2012: Tuning the climate of a global model. *J. Adv. Model. Earth Syst.*, **4**, M00A01, doi:10.1029/2012MS000154.
- Miura, H., M. Satoh, T. Nasuno, A. T. Noda, and K. Oouchi, 2007: A Madden–Julian Oscillation event realistically simulated by a global cloud-resolving model. *Science*, **318**, 1763–1765.
- Miyakawa, T., M. Satoh, H. Miura, H. Tomita, H. Yashiro, A. T. Noda, Y. Yamada, C. Kodama, M. Kimoto, and K. Yoneyama, 2014: Madden–Julian Oscillation prediction skill of a new-generation global model demonstrated using a supercomputer. *Nat. Commun.*, **5**, 3769, doi:10.1038/ncomms476.
- Möbis, B., and B. Stevens, 2012: Factors controlling the position of the intertropical convergence zone on an aquaplanet. *J. Adv. Model. Earth Syst.*, **4**, M00A04, doi:10.1029/2012MS000199.
- Nordeng, T.-E., 1994: *Extended versions of the convective parameterization scheme at ECMWF and their impact on the mean and transient activity of the model in the tropics*. ECMWF Tech. Memo., **206**, Eur. Cent. For Medium-Range Weather Forecasts, Reading, UK, doi:10.21957/e34xwhysw.
- Peters, K., C. Jakob, L. Davies, B. Khouider, and A. J. Majda, 2013: Stochastic behavior of tropical convection in observations and a multicloud model. *J. Atmos. Sci.*, **70**, 3556–3575.
- Peters, K., T. Crueger, C. Jakob, and B. Möbis, 2017: Improved MJO-simulation in ECHAM6.3 by coupling a stochastic multicloud model to the convection scheme. *J. Adv. Model. Earth Syst.*, **9**, 193–219.
- Randall, D., M. Khairoutdinov, A. Arakawa, and W. Grabowski, 2003: Breaking the cloud parameterization deadlock. *Bull. Amer. Meteor. Soc.*, **84**, 1547–1564.
- Rui, H., and B. Wang, 1990: Development characteristics and dynamic structure of tropical intraseasonal convection anomalies. *J. Atmos. Sci.*, **47**, 357–379.
- Satoh, M., T. Matsuno, H. Tomita, H. Miura, T. Nasuno, and S. Iga, 2008: Nonhydrostatic ICosahedral Atmospheric Model (NICAM) for global cloud resolving simulations. *J. Comput. Phys.*, **227**, 3486–3514.
- Slingo, J. M., K. R. Sperber, J. S. Boyle, J.-P. Ceron, M. Dix, B. Dugas, W. Ebisuzaki, J. Fyfe, D. Gregory, J.-F. Gueremy, J. Hack, A. Harzallah, P. Inness, A. Kitoh, W. K.-M. Lau, B. McAvaney, R. Madden, A. Matthews, T. N. Palmer, C.-K. Park, D. Randall, and N. Renno, 1996: Intraseasonal oscillations in 15 atmospheric general circulation models: Results from an AMIP diagnostic subproject. *Climate Dyn.*, **12**, 325–357.
- Sperber, K. R., 2004: Madden–Julian variability in NCAR CAM2.0 and CCSM2.0. *Climate Dyn.*, **23**, 259–278.
- Sperber, K. R., J. M. Slingo, P. M. Inness, and K.-M. Lau, 1997: On the maintenance and initiation of the intraseasonal oscillation in the NCEP/NCAR reanalysis and the GLA and UKMO AMIP simulations. *Climate Dyn.*, **13**, 769–795.
- Stevens, B., M. Giorgetta, M. Esch, T. Mauritsen, T. Crueger, S. Rast, M. Salzmann, H. Schmidt, J. Bader, K. Block, R. Brokopf, I. Fast, S. Kinne, L. Kornblueh, U. Lohmann, R. Pincus, T. Reichler, and E. Roeckner, 2013: Atmospheric component of the MPI-M earth system model: ECHAM6. *J. Adv. Model. Earth Syst.*, **5**, 146–172.
- Subramanian, A. C., and T. N. Palmer, 2017: Ensemble superparameterization versus stochastic parameterization: A comparison of model uncertainty representation in tropical weather prediction. *J. Adv. Model. Earth Syst.*, **9**, 1231–1250.
- Thayer-Calder, K., and D. A. Randall, 2009: The role of convective moistening in the Madden–Julian oscillation. *J. Atmos. Sci.*, **66**, 3297–3312.
- Thual, S., A. J. Majda, and S. N. Stechmann, 2014: A stochastic skeleton model for the MJO. *J. Atmos. Sci.*, **71**, 697–715.
- Tian, B., D. E. Waliser, E. J. Fetzer, B. H. Lambrigtsen, Y. L. Yung, and B. Wang, 2006: Vertical moist thermodynamic structure and spatial-temporal evolution of the Madden–Julian Oscillation in atmospheric infrared sounder observations. *J. Atmos. Sci.*, **63**, 2462–2485.
- Tiedtke, M., 1989: A comprehensive mass flux scheme for cumulus parameterization in large-scale models. *Mon. Wea. Rev.*, **117**, 1779–1800.
- Tseng, K.-C., C.-H. Sui, and T. Li, 2015: Moistening processes for the Madden–Julian Oscillations during DYNAMO/CINDY. *J. Climate*, **28**, 3041–3057.
- Tseng, W.-L., B.-J. Tsuang, N. S. Keenlyside, H.-H. Hsu, and C.-Y. Tu, 2015: Resolving the upper-ocean warm layer improves the simulation of the Madden–Julian oscillation. *Climate Dyn.*, **44**, 1487–1503.
- Waliser, D. E., M. W. Moncrieff, D. Burridge, A. H. Fink, D. Gochis, B. N. Goswami, B. Guan, P. Harr, J. Heming, H.-H. Hsu, C. Jakob, M. Janiga, R. Johnson, S. Jones, P. Knippertz, J. Marengo, H. Nguyen, M. Pope, Y. Serra, C. Thorncroft, M. Wheeler, R. Wood, and S. Yuter, 2012: The “year” of tropical convection (May 2008–April 2010): Climate variability and weather highlights. *Bull. Amer. Meteor. Soc.*, **93**, 1189–1218.
- Waliser, D. E., K. Sperber, H. Hendon, D. Kim, M. Wheeler, D. Waliser, K. Sperber, L. Livermore, H. Hendon, D.

- Kim, E. Maloney, M. Wheeler, K. Weickmann, C. Zhang, L. Donner, J. Gottschalck, W. Higgins, I.-S. Kang, D. Legler, M. Moncrieff, S. Schubert, W. Stern, F. Vitart, B. Wang, W. Wang, and S. Woolnough, 2009: MJO simulation diagnostics. *J. Climate*, **22**, 3006–3030.
- Wang, B., and X. Xie, 1997: Coupled modes of the warm pool climate system. Part I: The role of air-sea interaction in maintaining Madden–Julian oscillation. *J. Climate*, **11**, 2116–2135.
- Wang, B., and G. Chen, 2017: A general theoretical framework for understanding essential dynamics of Madden–Julian oscillation. *Climate Dyn.*, **49**, 2309–2328.
- Wang, B., and S.-S. Lee, 2017: MJO propagation shaped by zonal asymmetric structures: Results from 24-GCM simulations. *J. Climate*, **30**, 7933–7952.
- Wang, B., F. Liu, and G. Chen, 2016: A trio-interaction theory for Madden–Julian oscillation. *Geosci. Lett.*, **3**, 34, doi:10.1186/s40562-016-0066-z.
- Wang, B., S.-S. Lee, D. E. Waliser, C. Zhang, A. Sobel, E. Maloney, T. Li, X. Jiang, and K.-J. Ha, 2018: Dynamics-oriented diagnostics for the Madden–Julian oscillation. *J. Climate*, **31**, 3117–3135.
- Wang, S., A. H. Sobel, and J. Nie, 2016: Modeling the MJO in a cloud-resolving model with parameterized large-scale dynamics: Vertical structure, radiation, and horizontal advection of dry air. *J. Adv. Model. Earth Syst.*, **8**, 121–139.
- Weickmann, K. M., G. R. Lussky, and J. E. Kutzbach, 1985: Intraseasonal (30–60 day) fluctuations of outgoing longwave radiation and 250 mb streamfunction during northern winter. *Mon. Wea. Rev.*, **113**, 941–961.
- Wheeler, M., and G. N. Kiladis, 1999: Convectively coupled equatorial waves: Analysis of clouds and temperature in the wavenumber-frequency domain. *J. Atmos. Sci.*, **56**, 374–399.
- Wheeler, M. C., and H. H. Hendon, 2004: An all-season real-time multivariate MJO index: Development of an index for monitoring and prediction. *Mon. Wea. Rev.*, **132**, 1917–1932.
- Yoneyama, K., C. Zhang, C. N. Long, 2013: Tracking pulses of the Madden–Julian oscillation. *Bull. Amer. Meteor. Soc.*, **94**, 1871–1891.
- Zhang, C., 2005: Madden–Julian Oscillation. *Rev. Geophys.*, **43**, RG2003, doi:10.1029/2004RG000158.
- Zhang, C., 2013: Madden–Julian oscillation: Bridging weather and climate. *Bull. Amer. Meteor. Soc.*, **94**, 1849–1870.
- Zhang, C., and M. Dong, 2004: Seasonality of the Madden–Julian oscillation. *J. Climate*, **17**, 3169–3180.